# Interfacial Ferroelectricity by van der Waals Sliding

**Authors:** M. Vizner Stern,[1] Y. Waschitz,[1] W. Cao, [2] I. Nevo,[1] K. Watanabe,[3] T. Taniguchi,[3] E. Sela,[1] M. Urbakh,[2] O. Hod,[2] M. Ben Shalom[1]*

**Affiliations:** [1] School of Physics and Astronomy, Tel Aviv University, Israel

[2] Department of Physical Chemistry, School of Chemistry, The Raymond and Beverly Sackler Faculty of Exact Sciences and The Sackler Center for Computational Molecular and Materials Science, Tel Aviv University, Tel Aviv 6997801, Israel.

[3] National Institute for Material Science, Tsukuba, Japan

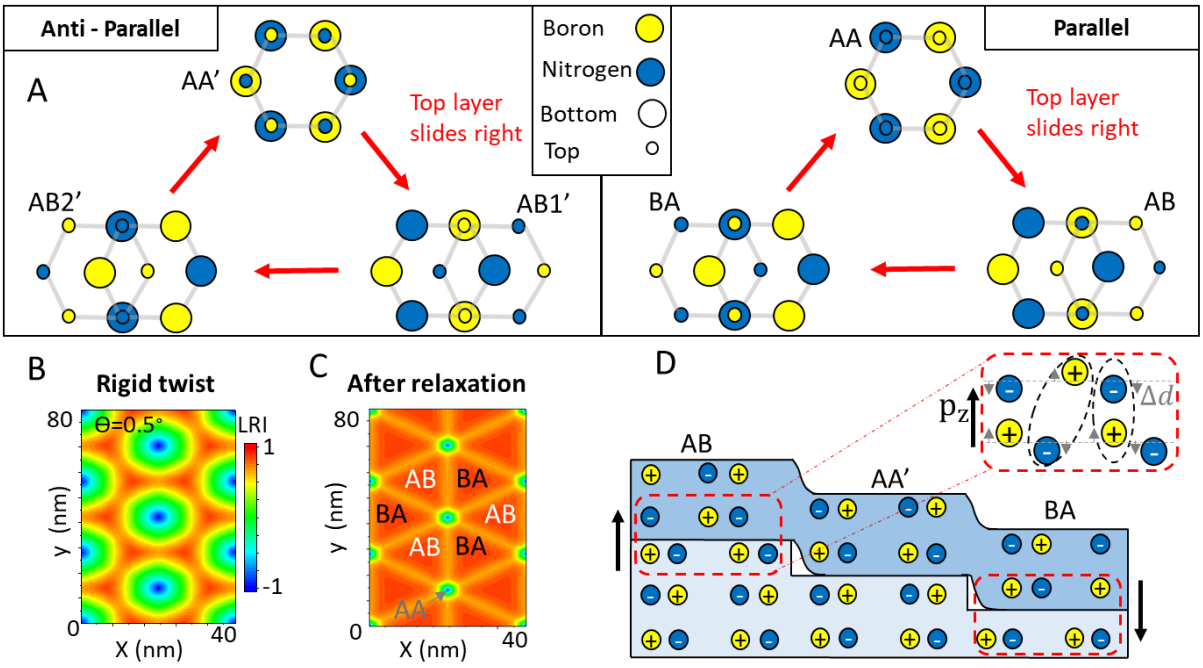


**Fig. 1. High symmetry interlayer stacking configurations.** (A) Top view illustration of two layers. For clarity, atoms of the top layer are represented by smaller circles. Within each group of parallel / anti-parallel twist orientations, a relative lateral shift by one lattice spacing results in a cyclic switching between three high-symmetry stacking configurations. (B) Calculated local-registry index (LRI) map of the atomic overlaps, see (*17*), in a rigid structure made of two *h*BN layers stacked with a twist angle of 0.5°. Blue regions correspond to AA stacking, whereas AB/BA stacking appear in orange (LRI = 0.86). (C) Calculated LRI map after geometry relaxation of the structure presented in (B). Large domains of uniform untwisted AB/BA stacking appear, at the expense of the pre-optimized AA regions. The twist is accumulated in smaller AA–like regions and in the ~ 10 nm wide incommensurate domain walls (bright lines), see Fig. S3 and (*17*) for further discussion. (D) Cross-sectional illustration of two few-layered flakes (blue and light blue regions marked the top and bottom flakes, respectively) of naturally grown *h*-BN (AA'), which are stacked with no twist. Plus (minus) signs mark boron (nitrogen) sites. A topographical step of a single layer switches between parallel and anti-parallel stacking orientations at the interface between the two flakes. Vertical charge displacements and the resulting net polarization $P_z$ are marked by arrows.

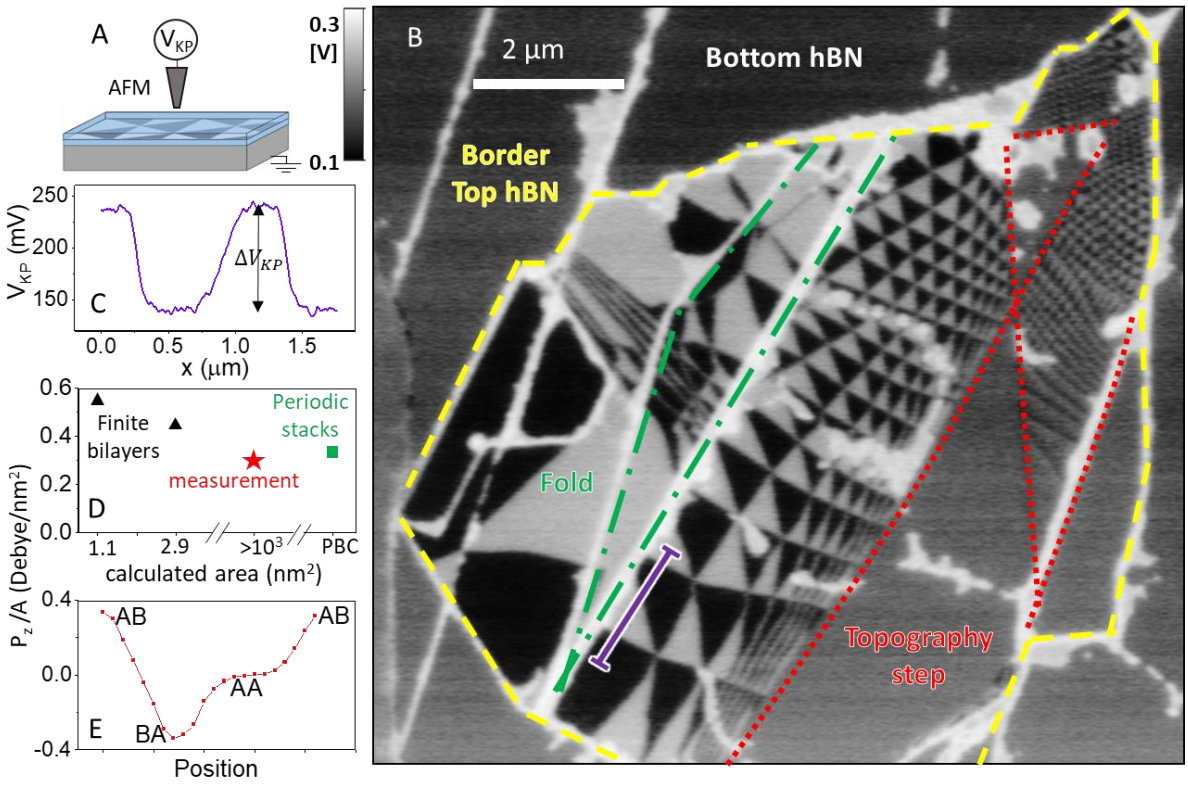


**Fig. 2. Direct measurement of interfacial polarization.** (A) Illustration of the experimental setup. An atomic force microscope is operated in Kelvin-probe mode to measure the local potential modulation, $V_{KP}$, at the surface of two 3 nm thick *h*-BN flakes, which are stacked with a very small twist angle. (B) $V_{KP}$ map showing oppositely-polarized domains of AB/BA stacking (black and white), ranging in area between ~0.01 and 1 µm$^2$ and separated by sharp domain-walls. (C) Surface potential measured along the purple line marked in (B) by first-harmonic KPFM. (D) DFT calculations of the polarization, $P_z$, per unit area obtained for finite *h*-BN bilayer flakes of different lateral dimensions ($1.1$ and $2.9$ $\mathrm{nm}^2$, black triangles) and for laterally periodic stacks made of 2-10 layers (marked as PBC, green square). The red star marks the polarization value evaluated from the measured $\Delta V_{KP}$ data. (E) Calculated polarization for different interlayer shifts.

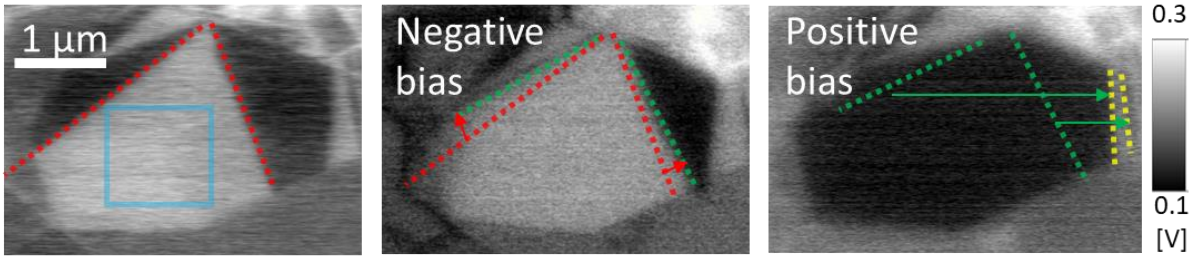


**Fig. 3. Dynamic flipping of polarization orientation by domain-wall sliding.** Kelvin-probe maps measured consecutively from left to right above a particular flake location showing domains of up (white) and down (black) polarizations. The middle image was taken after biasing the tip by a fixed DC voltage of -20 Volts and scanning it above the blue square region shown on the left-hand image. Then the tip was biased by 10 Volt and scanned again over the same region before taking the right-hand image. Consecutive domain-walls positions are marked by dashed red, green, and yellow lines. Larger white (black) domains appear after positive (negative) bias scans as a result of domain-wall motion beyond the scan area. Note that the number of domain-walls is apparently not altered.

Science
AAAS

# Supplementary Materials for

**Interfacial Ferroelectricity by van der Waals Sliding**

M. Vizner Stern,[1] Y. Waschitz,[1] W. Cao, [2] I. Nevo,[1] K. Watanabe,[3] T. Taniguchi,[3] E. Sela,[1] M. Urbakh,[2] O. Hod,[2] M. Ben Shalom[1]*

Correspondence to: moshebs@tauex.tau.ac.il

**This PDF file includes:**

## Materials and methods

### a) Device fabrication

*h*-BN flakes of various thicknesses are exfoliated onto a $SiO_2$ surface. A particular flake, 1-10 nm thick, is selected to have several topographic steps. AFM is used to scan the flake's topography to distinguish the parts made of even or odd number of layers. Subsequently, the flake is ripped off into two pieces, which are stacked together by a polymer stamp (*42*). We control the twist angle during the stamping process (0° or 180°) to determine the parallel/antiparallel interface orientations at different locations along the flake, based on the even/odd topography. Finally, the two-flakes-sandwich is placed on a graphite flake, Si\$SiO_2$ or a gold substrate.

### b) AFM measurements

Topography and Kelvin probe force microscopy (KPFM) measurements are acquired simultaneously (see Fig. S2), using Park System NX10 AFM in a non-contact scanning mode. The electrostatic signal is measured in the first harmonic or a sideband frequency using a built-in lock-in amplifier as detailed below. We use Multi-75g and PPP-EFM n-doped tips with a conductive coating. The mechanical resonance frequency of the tips is ~75 kHz, and the force constant is 3 N/m. The cantilever oscillates mechanically with an amplitude ranging from 20 to 5 nm. In several experiments, the average height above the surface, *h*, is controlled via a two-pass measurement. The first pass records the topography, whereas in the second pass, the tip follows the same scanline with a predefined lift (typically 5-50 nm) and measures the KPFM signal. In these two-pass experiments, we made sure to extend the lift beyond the mechanical oscillation amplitude. The cantilever is also excited with an AC voltage to perform KPFM measurements via first-harmonic, sideband, and open-loop methods (described below), with an amplitude of 1-6 V and frequency of 3-17 kHz. In the closed-loop measurements, the DC voltage is controlled by a servo motor to obtain the surface potential measurements. The images are acquired using Park SmartScan software, and the data analysis is performed with Gwyddion program.

To switch the domain orientation, biased scans are performed in a pin-point mode. Here, the tip approaches the surface vertically at each pixel in the scanned area. The estimated maximum force during this approach is 50nN. This mode minimizes lateral forces between the tip and the surface. We performed biased scans in different orientations (from right to left, up to down, and vice versa).

### c) Kelvin-probe surface potential measurements

First harmonic measurements

The applied voltage on the tip consists of DC and AC components. The voltage difference between the tip and the substrate electrode is given by (*43*) :

$$V = V_{\mathrm{DC}} + V_{\mathrm{AC}} \sin(\omega_e t) + V_{\mathrm{CPD}}, \tag{S1}$$

where $V_{\mathrm{CPD}}$ is the contact potential difference originating from the different work functions of the tip and the substrate plus the voltage drop at the *h*-BN interface. The force acting on the tip is:

$$F = -\frac{\partial U}{\partial z} = -\frac{\partial}{\partial z}\left(\frac{1}{2} C V^2\right) = F_s + F_{2\omega_e} - \frac{\partial C}{\partial z}(V_{CPD} + V_{DC}) V_{AC} \sin(\omega_e t), \tag{S2}$$

where $U$ is the electrostatic energy, $z$ is the distance between the sample and the tip, $C$ is the capacitance, $F_s$ is a static component and $F_{2\omega_e}$ is the second harmonic oscillation of the force. This claim holds assuming the sample is neutral and the field outside the sample due to the charge distribution in the sample is zero. The first harmonic

of the force vanishes for $V_{DC} = -V_{CPD}$. Hence, the principle of this KPFM mode is to apply a closed-loop DC voltage ($V_{DC}$) that nullifies this term. This DC voltage is recorded and plotted in Fig. 2B.

Sideband measurements

The scanning tip is composed of the conducting apex, a cone, and a cantilever. The latter two interact electrically with the surface on many-micrometer scale, average $V_{CPD}$ and therefore suppress its variations measurements in the first harmonic. To gain a more localized response, one may use the shifts at the mechanical resonance of the tip. The distance between the sample and the tip is typically dominated by mechanical oscillations: $z = h + A_m \cos(\omega_m t)$, with $\omega_m > \omega_e$ is the mechanical frequency and $A_m$ is the corresponding amplitude. Evaluating Eq. S2 up to the second derivative of $C$ (or, up to the force gradient), creates additional mechanical response at a sideband frequency ($\omega_m \pm \omega_e$) (*44*). This higher derivative term is enhanced for the electrode parts with the smallest $z$, making the sideband signal mostly affected by the apex (which is the closest part to the surface). Similarly, to the first harmonic, the sideband term is also proportional to $V_{CPD} + V_{DC}$. Thus, by nullifying the sideband response with a closed-loop DC voltage $V_{DC}$, one can measure the local surface potential (*45*).

We note that we only analyze the potential drop between two adjacent and uniform domains. Any global external contribution hence, should underestimate the measured $\Delta V_{KP}$ value. Indeed, we find a reduced value of $\Delta V_{KP} \sim 110\ mV$, measured by the first harmonic response (See Fig. 2C), while the sideband measurements suggest values in the range $200 - 230\ mV$ (see Fig. S1).

**d) Model system and classical force-field calculations**

To study the structural properties of twisted *h*-BN interfaces we constructed a model system consisting of two *h*-BN layers with an interlayer misfit angle of ~0.5°. To mimic the experimental scenario, a laterally periodic supercell was constructed with a triangular lattice of periodicity $L = |n\vec{a}_1 + m\vec{a}_2|$, where the primitive lattice vectors are given by $\vec{a}_1 = a_{hBN}(\sqrt{3}, 0)$ and $\vec{a}_2 = \frac{a_{hBN}}{2}(\sqrt{3}, 3)$, and the lattice constant, $a_{hBN} = 2.505$ Å, is obtained from the equilibrium boron-nitrogen bond-length used in the Tersoff potential, $b_{BN} = 1.446$ Å. The indices $n = 195$ and $m = 1$ were chosen to fulfill the condition:

$$\cos(\theta) = \frac{2n^2 - m^2 + 2n \cdot m}{2(n^2 + m^2 + n \cdot m)}. \quad \text{(S3)}$$

The corresponding moiré pattern dimension is $L = \frac{b_{BN}}{\sqrt{2 - 2\cos(\theta)}} = 16.3$ nm. The parallelepiped supercell was then multiplicated to construct a rectangular supercell consisting of more than 300,000 atoms.

The structural properties of the twisted *h*-BN interface were calculated using the Tersoff (*46*) intra-layer potential in conjunction with the recently developed dedicated interlayer potential (ILP) (*18*).

We first optimized the geometry of the top layer atoms with fixed supercell size using the Fire algorithm and keeping the bottom layer rigid. This was followed by optimization of the supercell dimensions by the conjugate gradient (CG) algorithm while scaling the rigid bottom layer according to the simulation box size. This two-step energy minimization procedure was repeated ten times, which is sufficient to obtain well converged results (see Fig. S3C). In each repetition, both minimization stages were terminated when the forces acting on each degree of freedom reduced below $10^{-3} eV/\text{Å}$. The system was further relaxed by the Fire algorithm at a force tolerance of $10^{-4} eV/\text{Å}$. The optimized structure exhibits atomic reconstruction with distinct AB and BA stacking domains separated by domain walls (see Fig S3A).

**e) <u>Local registry index analysis</u>**

The local registry index (LRI) (see Fig. 1D) is a method introduced to quantify the degree of local interfacial registry matching at rigid material interfaces (*47*, *48*). The idea is to assign a number between -1 and 1 to each atom in the layer, signifying whether it resides in an optimal or worse stacking region, respectively. To this end, a circle is associated with each atomic position in the two layers and the overlaps between circles of one layer and those of the adjacent layer are evaluated. For the case of *h*-BN three types of overlaps are considered, namely $S_i^{NN}$, $S_i^{NB} = S_i^{BN}$, and $S_i^{BB}$. Here, $S_i^{JK}$ signifies the overlap of the circle associated with atom $i$ of type $J$ in one layer with all circles associated with $K$ type atoms in the adjacent layer. The radius of the circles associated with B and N atoms is taken as $r_{\mathrm{B}} = 0.15 b_{hBN}$, and $r_{\mathrm{N}} = 0.5 b_{hBN}$, which provides good qualitative agreement between registry index maps and sliding potential energy surfaces obtained from density functional theory calculations (*47*). The LRI of atom *i* is then defined as the average registry index of itself and its three nearest neighbors (*j*, *k*, *l*) within the entire layer, as follows:

$$LRI_i = \frac{1}{3}\sum_{n=j,k,l} \frac{\left[\left(S_i^{NN}+S_n^{NN}\right)-\left(S_i^{NN,opt}+S_n^{NN,opt}\right)\right]+\left[\left(S_i^{BB}+S_n^{BB}\right)-\left(S_i^{BB,opt}+S_n^{BB,opt}\right)\right]-\left[\left(S_i^{NB}+S_n^{NB}\right)-\left(S_i^{NB,opt}+S_n^{NB,opt}\right)\right]}{\left[\left(S_i^{NN,worst}+S_n^{NN,worst}\right)-\left(S_i^{NN,opt}+S_n^{NN,opt}\right)\right]+\left[\left(S_i^{BB,worst}+S_n^{BB,worst}\right)-\left(S_i^{BB,opt}+S_n^{BB,opt}\right)\right]-\left[\left(S_i^{NB,worst}+S_n^{NB,worst}\right)-\left(S_i^{NB,opt}+S_n^{NB,opt}\right)\right]}, \quad \text{(S4)}$$

where $S_i^{JK,opt}$ and $S_i^{JK,worst}$ are $S_i^{JK}$ are evaluated at the optimal and worst local stacking modes, respectively (AA' and AA in the case of *h*-BN, respectively, see Fig 1A of the main text). The calculated $LRI_i$ is then transformed by $-(2LRI_i - 1)$ to make it range be between [-1, 1]. With this, the LRI at an AA' (AA) stacked region is 1 (-1) respectively, and that of an AB stacked region is 0.86.

Plotting the LRI following geometry relaxation as discussed above (see main text Fig. 3D) we found an ordered array of AB and BA stacked domains separated by sharp domain walls. To estimate the width of the domain-wall region, we plotted a cross section of the out-of-plane height profile (see Fig. S3D) along the path marked by the dashed black line in Fig. S3B. A clear inverse correlation between the height map (red line) and the registry index (black line) is obtained. At the AB and BA stacked regions the interlayer distance is relatively constant at ~3.23 Å and correspondingly a relative constant value of LRI ~0.86 is obtained. At the center of the domain wall, the interlayer distance increases by ~0.05 Å and the LRI reduces to ~0.67, whereas at the domain wall crossings the interlayer distance reaches ~3.57 Å and the LRI drops to ~-0.93. Using a Gaussian fitting to the height profile near the domain wall we can estimate the domain wall width to be ~10 nm.

**f) Dipole moment calculations**

1. Finite systems calculations

To evaluate the dipole moment developing in the system we first considered a finite AB stacked hexagonal *h*-BN bilayer model with a surface area of 1.1 $nm^2$ and armchair edges. The flake was initially constructed with uniform B-N bond lengths of 1.446 Å and the edges were saturated by hydrogen atoms with initial B-H and N-H bond lengths of 1.200 Å and 1.020 Å, respectively (see Fig. S4A,C). The structures were optimized using density functional theory (DFT) calculations applying the hybrid B3LYP exchange-correlation density functional approximation and the double-ζ polarized 6-31G** Gaussian basis set (*49*) as implemented in the Gaussian 16 suite of programs (*50*). This was followed by refined relaxation adding Grimme's D3 dispersion correction (*51*) and using the 6-31+G** basis set. Finally, single point calculations were performed on the minimized structures at the B3LYP/6-31+G** and B3LYP/Def2TZVP (*52*) level of theory. Comparison of the out-of-plane dipole moment components obtained using the three basis sets is provided in Table S1, showing that our results are well converged with respect to basis set size. The value calculated by Def2TZVP was used in Fig. 1C in the main text. Table S1, displays also the in-plane dipole moments, which are found to be an order of magnitude lower that the corresponding out-of-plane component.

To verify that the flake size used is sufficiently large, we repeated the dipole moment calculation for a bilayer flake with surface area of 2.9 $nm^2$. As can be seen in Table S1 the obtained values are within 20-25% with those of the smaller flake. This indicates that the qualitative nature of the system's polarization is already captured at the smaller flake size, however, for quantitative analysis, larger systems or periodic boundary conditions calculations are require.

**Table S1.** The dipole moment calculated for the finite flake models along the out-of-pane ($P_z$), and in-plane ($P_x$ and $P_y$) directions.

| | Area ($nm^2$) | Dipole moment (Debye/$nm^2$) | | | | |
|---|---|---|---|---|---|---|
| | | 6-31G** | 6-31+G** | Def2TZVP | | |
| | | $P_z$ | $P_z$ | $P_z$ | $P_x$ | $P_y$ |
| Double layer | 1.1 | 0.66 | 0.55 | 0.55 | 0.0 | 0.044 |
| | 2.9 | 0.52 | 0.45 | 0.45 | -0.0006 | 0.046 |

2. Periodic structure

2.1 Geometry optimization.

Based on the finite system calculations we repeated the dipole moment calculations in periodic bilayer and multilayer systems. For the bilayer systems, we chose a unit cell consisting of two nitrogen and two boron atoms stacked at several stacking modes. The geometry of the initial structure was optimized using the Vienna Ab-initio

Simulation Package (VASP) (*53*) with the Perdew-Burke Ernzerhof (PBE) exchange-correlation functional approximation (*54*). Three-dimensional periodic boundary conditions were applied using a 10 nm vacuum gap in the vertical direction to avoid interactions between adjacent bilayer images. The core electrons of the boron and nitrogen atoms were treated via the projector augmented wave (PAW) and pseudopotential approach (*55*). The van der Waals interaction was incorporated via the many-body dispersion (MBD) approach (*56*). During optimization, both the cell box and the coordinates of the ions were allowed to relax, while keeping the size of the vacuum fixed. The energy cut-off was set to 850 eV during geometry optimization. The conjugate-gradient algorithm was applied with a force tolerance of 0.01 eV/Å. The Brillouin zone was sampled with a Gamma-centered 15×15×1 *k*-mesh.

Convergence tests with respect to the vacuum size, energy cut-off, and number of reciprocal space k-points indicate that our choice of parameters leads to total energies converged to within 0.005, 0.0003, and 0.0002 eV with respect to the vacuum size, energy cutoff, and number of k-points, respectively (see Fig. S5).

2.2 Dipole moment.

The dipole moment of the bilayer system at various stacking modes was evaluated using three methods: (i) the Berry phase method implemented in VASP to circumvent the effect of the vertical periodic boundary conditions; (ii) integration of the charge density differences between the bilayer system and the individual layers, which are non-polar in the vertical direction. To this end, the charge density differences were first integrated over the lateral directions, the result was then multiplied by the z-coordinate value and integrated vertically; (iii) using the Gaussian 16 package (*50*) that evaluates the dipole moment with two-dimensional periodic boundary conditions, thus avoiding the need for Berry phase corrections. Here, single-point calculations on the optimized structures obtained using VASP were performed with the PBE functional and the triple-$\zeta$ pob-TZVP basis set with a uniform 10x10 k-point mesh to obtain converged electron density and dipole moment. The direct comparison between the three approaches is discussed in section f2.3.

The consistency of our results is verified by the fact that the dipole moments evaluated via the periodic boundary conditions calculations are comparable to those obtained for the finite flakes (see section f1 above and Fig. 1C of the main text). Furthermore, a clear trend of reduction of the out-of-plane polarization with system size (probably due to reduced contribution of charge polarization at the edges - see Fig. S4B and D) is found where the value obtained using periodic boundary conditions calculations are in good agreement with the experimental value measured for extended micrometer-scale domain regions (see Fig. 1C of the main text).

To characterize the stacking mode dependence of the polarization (see Fig.1 of the main text), the top layer of the bilayer *h*-BN was shifted along the armchair direction with steps of 0.2 Å, starting from the optimized AB stacking configuration going through the AA and BA stacking modes and arriving back at AB stacking. At each relative interlayer displacement the in-plane coordinates of the ions were fixed, and their out-of-plane coordinate was allowed to relax following the procedure detailed in section f2.1 above. For comparison purposes single-point rigid shift polarization calculations were also performed by fixing the interlayer distance at 3.3 Å completely neglecting atomic relaxation effects. The results presented in Fig. S6 demonstrate that the calculated polarization in practically insensitive to out-of-plane atomic relaxation effects.

2.3 Stack thickness effect.

Since the experimental measurements are performed on multilayer *h*-BN stacks, we explored the thickness effect on the calculated polarization of AB-stacked *h*-BN (Fig. S7A) using the three different methods described in section f2.2 above. To this end, we constructed multilayer *h*-BN models, where the entire structure is stacked in the AA' stacking mode, apart from one AB stacking fault introduced between the two central layers, such that the numbers of layers above and below the stacking fault are the same. The results from VASP (both the berry phase method and integration of charge density difference) shows a slightly increase of $p_z$ with the thickness, which is mainly due to reduction of the vacuum region with increased model thickness. The change of $p_z$ as a function of the vacuum size calculated by berry phase method for bilayer *h*-BN is plotted to support this statement (see Fig. S7B). The results calculated by Gaussian presented in Fig. S7A and C show that the out-of-plane polarization and potential drop between the upper and lower surfaces are nearly independent of the number of layers (for both rigid and flexible shifts – see section f2.2 above) indicating that the main contribution to the system's polarization originates from the AB stacked interface. This is further supported by the charge density differences (with respect to the individual layers) analysis along the out-of-plane direction presented in Fig. S7D. The charge variations are found to mainly occur at the central AB stacked *h*-BN interface, regardless of the number of layers in the system. The profiles shown here are consistent with the qualitative behavior appearing in recent publications (*57*). We note that the polarization reported herein is about half of the values presented in these references for an *h*-BN bilayer (*11*, *57*). This might be attributed to differences in the calculation parameters, such as the vacuum size and reciprocal-space sampling (which we have carefully tested for convergence, see section f2.1 above) or the use of vdW correction along the out-of-plane direction. A more detailed representation of the charge density differences is given in Fig. S8, where a two-dimensional cross section along the (110) crystallographic direction of the AB stacked bilayer *h*-BN is presented. Charge tends to accumulate atop the nitrogen ions that reside above hexagon centers of the adjacent layer. It is this charge redistribution that produces the intrinsic out-of-plane dipole moment of the system.

To further support our claim that the polarization originates from the AB stacked interface, we constructed multilayer structures in which all adjacent layers are AB stacked. The calculated out-of-plane polarization of the system as a function of number of layers is presented in Fig. S9 (red squares). The results of Fig. S7A are presented as well (red circles) for comparison purposes. We find that the dipole moment of the fully AB stacked multilayer scales linearly with the number of layers, where the slope is given by the polarization of the bilayer model. This proves that indeed the polarization originates from the AB stacked interface and offers a simple route to increase the magnitude of the polarization of the system.

2.4 Effect of external electric field.

To evaluate the effects of the electric fields applied perpendicular to the layered interface in the experimental setup, we performed DFT calculations on the AB-stacked double layer *h*-BN under electric fields in the range 0.01 to 0.1 $V/nm$, relevant to the experiment. The field was applied perpendicular to the interface in both the positive and the negative directions. At each field, geometry optimization was performed following the procedure detailed in section f2.1. The field induced dipole moment (obtained using method (iii) of section f2.2), total energy, and interlayer distance variations are presented in panels A and B of Fig. S10. The results show that positive electric fields result in reduction of the perpendicular dipole moment accompanied by slight

destabilization of the double layer structure and increase of the interlayer distance. This agrees with our finding of a permanent dipole moment appearing at AB stacked *h*-BN interfaces even in the absence of external fields.

**g) Minimalistic classical cohesive energy model**

1. Model description

Our minimalistic model provides a classical estimate of the out-of-plane polarization of the AB bilayer interface treating the boron and nitrogen atoms as point charges (see Fig. S11A,B), interacting via Pauli and van der Waals (VdW) forces (described by the Lennard-Jones (LJ) potential), and Coulomb interactions. The total interlayer energy is written as follows:

$$E = \frac{1}{2}\sum_{i,j}\left[4\varepsilon\left(\left(\frac{\sigma}{r_{ij}}\right)^{12} - \left(\frac{\sigma}{r_{ij}}\right)^{6}\right) + \frac{q_i q_j}{r_{ij}}\right], \quad \text{(S5)}$$

where $\varepsilon$ is the cohesive energy with $\sigma \equiv 3.3$ Å. We note that realistic models of *h*-BN should take atom specific $\varepsilon$ and $\sigma$ values. Here, however we are interested in a qualitative description of the system and hence, for simplicity, we limit the treatment for uniform parameter values. The differences in electronegativity of the boron and nitrogen atoms are effectively taken into account by assigning dimensionless partial charges located at the nuclear centers $q = \pm q_i/e$ for $i \in B, N$ respectively. The parameter $q^2/\epsilon\sigma$ controls the relative strength between the Coulomb and LJ interactions. As we will demonstrate, this competition determines the sign of the polarization at the AB interface. We denote by α the atomic sites in one layer that reside above hexagon centers in the other layer (termed herein as hollow sites). Correspondingly, $\beta$ denotes atomic sites in one layer that reside above oppositely charged sites on the adjacent layer (termed herein as eclipsed sites). In each layer we use $h_\alpha$ or $h_\beta$ to denote vertical heights of α and $\beta$ atomic sites, measured with respect to the midplane of the AB interface. To compute the polarization, we minimize the classical energy with respect to $h_\alpha$ and $h_\beta$, via an approximate two-step protocol:

1. First, we set $h_\alpha = h_\beta = h/2$ and minimize the interaction energy with respect to $h$.
2. Then we allow for finite relative vertical motion of B-N pairs around the optimal $h$ value $2\Delta d = h_\alpha - h_\beta$, which generates the polarization. Note that no lateral atomic motion is allowed.

2. Optimal interlayer spacing at the AA' stacking mode

As a reference, we first consider two *h*-BN layers in the AA' stacking configurations with $h_\alpha = h_\beta = h/2$. The total force per atom is:

$$F_{\mathrm{AA'}}(h) = -\frac{dE_{AA'}(h)}{dh} = F^{LJ}_{\mathrm{AA'}} + F^{C}_{\mathrm{AA'}} \quad \text{(S6)}$$

The Coulomb contribution can be written as $F^{C}_{\mathrm{AA'}} = -F^{C}_{11} + F^{C}_{12}$ (with $F^{C}_{11}, F^{C}_{12} > 0$), where

$$F^{C}_{11}(h) = \sum_{\vec{R}_{11}} \frac{e^2 h}{\left(\vec{R}^2_{11}+h^2\right)^{3/2}} \quad , \quad F^{C}_{12}(h) = \sum_{\vec{R}_{12}} \frac{e^2 h}{\left(\vec{R}^2_{12}+h^2\right)^{3/2}}. \quad \text{(S7)}$$

Here, $\vec{R}_{11} = \vec{R}_{n1,n2}$ denote in plane lattice vectors connecting equivalent atoms, namely Bravais lattice vectors, and $\vec{R}_{12} = \vec{R}_{n1,n2} - \hat{x}R_0$ denote in plane lattice vectors connecting inequivalent atoms, where $\hat{x}R_0$ is a vector connecting nearest-neighbors. The corresponding Bravais lattice vectors of the honeycomb lattice are given by $\vec{R}_{n_1,n_2} = n_1\vec{R}_1 + n_2\vec{R}_2$, and $\vec{R}_{1,2} = R_0(\frac{3}{2}, \pm\frac{\sqrt{3}}{2})$, with $R_0 = 1.4$ Å. Quick convergence of $F^{C}_{\mathrm{AA'}}$ is guaranteed if for any pair of integers $n_1, n_2$ the term $F^{C}_{11}(h)$ is combined with $F^{C}_{12}(h)$ calculated for $-n_1, -n_2$ and the sums are taken over the range $-n_m \le n_1, n_2 \le n_m$ with sufficiently large $n_m$. The force then converges as $1/n_m^2$ (not

shown) in Fig. S11C. Notably, the attractive force $e^2/h^2$ associated with a single vertical bond is strongly suppressed due to the alternating charges within the layer and the small ratio $R_0/h$. This reduces the bare Coulomb interlayer energy $\frac{e^2}{h} \sim 4.3$eV into the meV regime, comparable with the VdW scale $\varepsilon$ (*58*).

Similarly, the LJ force can be split as $F^{LJ}_{\mathrm{AA}'} = F^{LJ}_{11} + F^{LJ}_{12}$, where

$$F^{LJ}_{11}(h) = 4\varepsilon \sum_{\vec{R}_{11}} \left( \frac{12\sigma^{12}h}{\left(\vec{R}^2_{11}+h^2\right)^7} - \frac{6\sigma^6 h}{\left(\vec{R}^2_{11}+h^2\right)^4} \right), \quad F^{LJ}_{12}(h) = 4\varepsilon \sum_{\vec{R}_{12}} \left( \frac{12\sigma^{12}h}{\left(\vec{R}^2_{12}+h^2\right)^7} - \frac{6\sigma^6 h}{\left(\vec{R}^2_{12}+h^2\right)^4} \right). \tag{S8}$$

The zero-force condition yields the optimal interlayer distance $h$, marked in Fig. S11D by solid lines. As shown, $h$ decreases upon decreasing the Lenard-Jones energy scale $\varepsilon$ with respect to the Coulomb energy.

We note that a reasonable approximation for $F^{LJ}_{\mathrm{AA}'}(h)$, for small $R_0/h$, consists of treating the particles as a uniform mass distribution, i.e. replacing the sum over $\vec{R}$ by integration, yielding

$$F^{LJ}_{continuum}(h) = \lim_{R_0/h \to 0} F^{LJ} = \varepsilon \frac{32\pi}{3\sqrt{3}R_0^2} h \left( \frac{\sigma^{12}}{h^{12}} - \frac{\sigma^6}{h^6} \right). \tag{S9}$$

3. Optimal interlayer spacing at the AB stacking mode

Now consider two *h*-BN layers at the AB stacking configuration. The corresponding interlayer force can be written as $F_{AB} = F^{LJ}_{AB} + F^{C}_{AB}$. The unit cell consists of two types of atomic sites, one type where atoms of the two layers reside atop of each other (eclipsed) and the other type where an atom of one layer resides atop a hexagon center of the other layer (hollow sites). Note that the Coulomb contribution of the hollow sites vanishes due to symmetry considerations. Hence, we only have the Coulomb contribution from the eclipsed atomic sites. Since the latter have the exact same configuration in the AA' and AB stacking modes (see Fig. S11A) the overall Coulomb force contribution per atom in the AB stacking mode is half of that in the AA' mode, $F^{C}_{AB} = \frac{1}{2} F^{C}_{AA'}$.

For the VdW part, similar to the AA' stacking case, the eclipsed atomic sites give $F^{LJ}_{11} + F^{LJ}_{12}$ of Eq. S10, whereas the hollow atomic sites give $2F^{LJ}_{12}$ due to the unique symmetry of the AB stacked bilayer hexagonal lattice. Therefore, in total we obtain for the LJ force contribution per atom that $F^{LJ}_{AB} = \frac{F^{LJ}_{11}+F^{LJ}_{12}}{2} + \frac{2F^{LJ}_{12}}{2} = \frac{F^{LJ}_{11}}{2} + \frac{3F^{LJ}_{12}}{2}$. The zero-force condition yields the optimal AB stacking interlayer distance, marked by the dashed gray line in Fig. S11D. Similar to the case of AA' stacking mode, $h$ decreases upon decreasing $\varepsilon/q^2$. Note, however, that while $h$ (AA') > $h$ (AB) for large $\varepsilon/q^2$ the situation is inverted for $\frac{\varepsilon}{q^2} \lesssim 1.5$ meV. Specifically, when $q \to 0$ our model corresponds to the case of graphite with optimal AB stacking mode.

4. Relative vertical displacement

On top of the interlayer spacing, we now allow a small opposite motion of the hollow site ($\alpha$) and eclipsed site ($\beta$) atoms:

$$h_\alpha = h/2 + \Delta d, \quad h_\beta = h/2 - \Delta d, \tag{S10}$$

as marked in Fig. S11B. We now analyze the total energy of the system as a function of $\Delta d$, via the Harmonic approximation $E \cong const + \left(\frac{dE}{d(\Delta d)}\right)_{\Delta d=0} \Delta d + \frac{1}{2}\left(\frac{d^2E}{d(\Delta d)^2}\right)_{\Delta d=0} \Delta d^2$ around $\Delta d = 0$. The assumption that $\Delta d \ll R_0$ can be justified by the experimental estimate of $\Delta d \sim 10^{-3}$ Å (see main text). Our simple model considered

here, similar to an Einstein model for lattice vibrations, assumes that the $\Delta d$ coordinates are independent Harmonic oscillators with spring constant $K_{\Delta d} = \frac{d^2E}{d(\Delta d)^2}$. Crucially, $\Delta d = 0$ is not a minimum due to the reduced symmetry of the AB interface, with alternating eclipsed and hollow sites, which imposes a finite normal force (per atom) of:

$$F_{\Delta d} = -\frac{dE}{d(\Delta d)} = F_{\Delta d}^{C} + F_{\Delta d}^{LJ} \ , \tag{S11}$$

where $F_{\Delta d}^{C}$ and $F_{\Delta d}^{LJ}$ are defined as the relative displacement force contributions of the Coulomb and LJ terms. Note that $F_{\Delta d}$ is the difference between the forces acting on the eclipsed versus the hollow sites.

Since, for $\Delta d = 0$, hollow site atoms see a locally charge-neutral configuration on the other layer the Coulomb part of this linear force originates only from the eclipsed atomic sites. For the latter, the atom in the upper layer is attracted to the one residing exactly below it in the other layer. However, it is repelled by its next nearest neighbors in the other layer, and so on. When performing the entire lattice sum for the eclipsed site we obtain that the overall force is always attractive:

$$F_{\Delta d}^{C} = \frac{F_{11}^{C}(h) - F_{12}^{C}(h)}{2} > 0. \tag{S12}$$

On the other hand, the LJ potential, which can be written as the difference between the hollow site $\left(2F_{12}^{LJ}(h)\right)$ and the eclipsed site $\left(F_{11}^{LJ}(h) + F_{12}^{LJ}(h)\right)$ contributions yields a repulsive force per atom near the equilibrium interlayer distance:

$$F_{\Delta d}^{LJ} = \frac{2F_{12}^{LJ}(h)}{2} - \frac{F_{11}^{LJ}(h) + F_{12}^{LJ}(h)}{2} = \frac{F_{12}^{LJ}(h) - F_{11}^{LJ}(h)}{2} < 0. \tag{S13}$$

This signifies that at the equilibrium interlayer distance, the eclipsed site contribution is more repulsive than that of the hollow site counterpart, mainly due to the fact that the eclipsed atoms are forced to reside within the steep Pauli repulsion wall side of their pairwise interaction.

Overall, from Eqs. S11, S12 and S13 our crude estimate yields

$$\Delta d \sim \frac{F_{\Delta d}}{K_{\Delta d}} = \frac{\left(F_{11}^{C}(h) - F_{12}^{C}(h)\right) + \left(F_{12}^{LJ}(h) - F_{11}^{LJ}(h)\right)}{2K_{\Delta d}}. \tag{S14}$$

$K_{\Delta d}$ in Eq. (S14) can be evaluated from the model parameters (see next section). Nevertheless, for simplicity we take it to be equal to the corresponding out-of-plane force constant in graphite $K_{\Delta d} \sim 5$ N/m (*59*).

The resulting relative displacement is plotted in Fig. S11E versus $\varepsilon/q^2$. Crucially, it changes sign when $\varepsilon_{\text{eff}} = \frac{\varepsilon}{q^2} \sim 3.5$ meV. The experimentally measured voltages indicate that $\Delta d$ in AB stacked bilayer *h*-BN is of the order of $10^{-3}$ Å (see main text) and our DFT calculations indicate that it is positive suggesting that $\frac{\varepsilon}{q^2} \sim 3$ meV (see Fig. S11E), similar to expected values (*58*). Notably, other layered materials, which possess different effective $\varepsilon$ and or $q$ values may show different quantitative and even qualitative polarization.

Finally, it should be noted that our simplistic classical approach is sufficiently flexible to allow the study of additional effects, such as the dependence on the number of layers as well as external perturbations like pressure or electric field, as well as an additional in-plane component of the polarization, which we leave for future work.

5. Analytic estimate of the normal spring constant

To determine $K_{\Delta d} = \frac{d^2E}{d(\Delta d)^2}$, we note that it has contributions from the interlayer LJ and Coulomb forces, as well as from the intra-layer forces. Its interlayer LJ contribution is obtained from the corresponding contribution to the

energy $E^{LJ}(\Delta d)=\frac{1}{2}\left[V_{11}^{LJ}(h)+V_{12}^{LJ}(h-2\Delta d)\right]+\frac{1}{2}\left[V_{12}^{LJ}(h)+V_{12}^{LJ}(h+2\Delta d)\right]$. The first (second) term represents the interaction of atoms at eclipsed (hollow) sites, and $V_{11(12)}^{LJ}(h)=4\varepsilon\sum_{\vec{R}_{11(12)}}\left(\frac{\sigma^{12}}{\left(\vec{R}_{11(12)}^{2}+h^{2}\right)^{6}}-\frac{\sigma^{6}}{\left(\vec{R}_{11(12)}^{2}+h^{2}\right)^{3}}\right)$. One can obtain a good approximation for the spring constant $\left(\frac{d^{2}E}{d(\Delta d)^{2}}\right)_{\Delta d=0}$ by replacing the sums $\sum_{\vec{R}_{11(12)}}$ by integrals, as in $F_{continuum}^{LJ}(h)$ . This procedure yields:

$$K_{\Delta d}^{LJ}=\frac{64\pi}{\sqrt{3}R_{0}^{2}}\varepsilon. \tag{S15}$$

For $\varepsilon$=3meV this yields a spring constant of $K_{\Delta d}^{LJ}=3\ \mathrm{N/m}$. While additional contributions are expected from intra-layer interactions, as well as Coulombic inter-layer interactions, this value is comparable with the measured out-of-plane force constant in graphite $K_{\Delta d}$~5 N/m (*59*). Since Eq. S15 captures the order of magnitude of $K_{\Delta d}$, we can use $K_{\Delta d}=\frac{64\pi}{\sqrt{3}R_{0}^{2}}\varepsilon\cdot a$, with a factor of order unity $a\sim\frac{5}{3}$, and obtain an approximate expression for the relative displacement, see Eq. (S14), fully in terms of our model's parameters, $\Delta d\sim\frac{F_{\Delta d}}{K_{\Delta d}}=\frac{\sqrt{3}R_{0}^{2}}{32\pi}\frac{\left(F_{11}^{C}(h)-F_{12}^{C}(h)\right)+\left(F_{12}^{LJ}(h)-F_{11}^{LJ}(h)\right)}{4\varepsilon}$

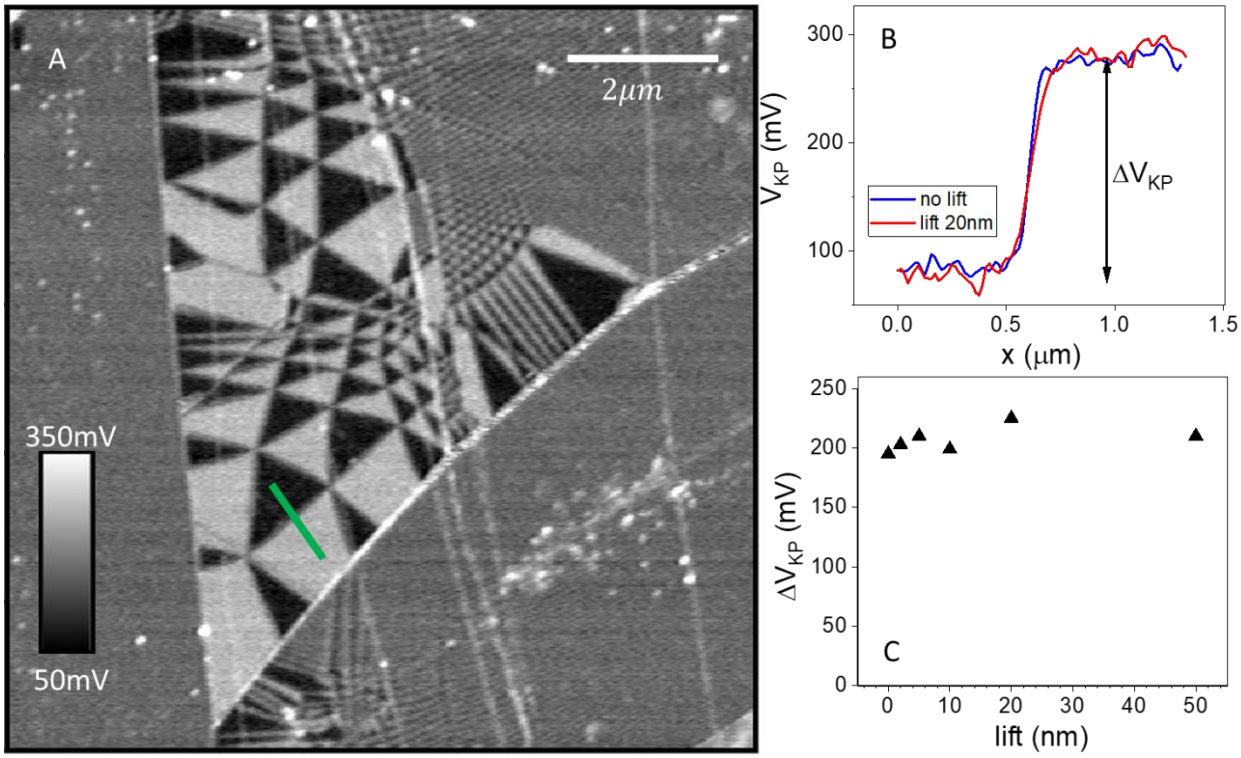


**Fig S1**. **Quantitative sideband KPFM measurements**. (A) Map of the surface potential in parallel stacked *h*-BN, measured from the response at a frequency of 68 kHz. The tip's mechanical resonant frequency is 71 kHz, and the electrical frequency is chosen to be 3 kHZ. The *h*-BN sandwich is 11 nm thick above the graphite substrate. (B) Surface potential along the green line marked in A. The blue line was taken in a single pass, whereas the red line was measured in a two-pass mode, with a lift of 20 nm above the first pass height. (C) $\boldsymbol{\Delta V_{KP}}$ (as marked in B) for different lifts.

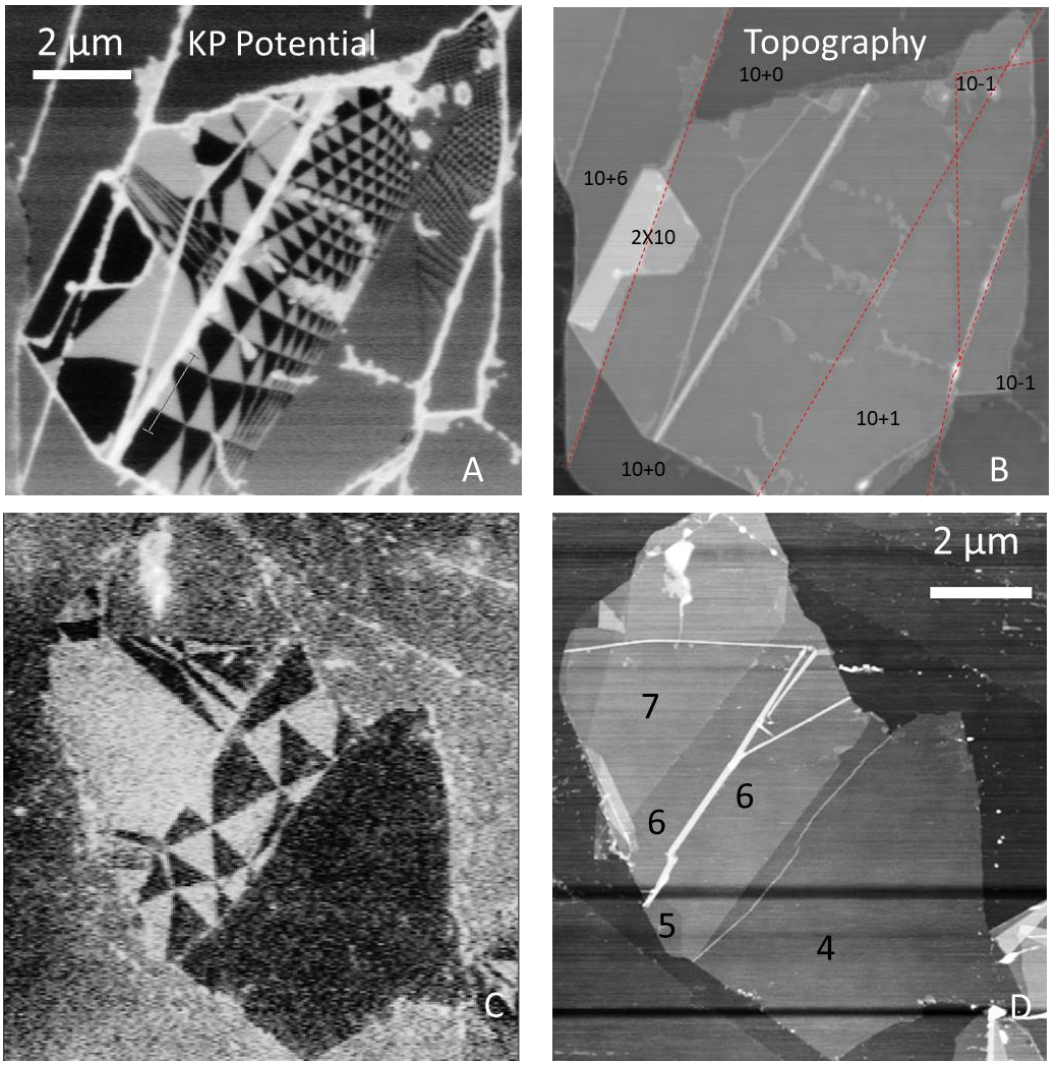


**Fig S2. Topography maps and additional samples.** (A, B) Surface potential and topography maps measured simultaneously on the structure presented in the main text (Fig 2B). The top *h*-BN flake thickness is uniform and includes 10 layers. Topography steps in the surface of the bottom flake are marked by dashed red lines, and its total thickness at different positions is indicated. (C, D) An additional interface between a thick (>1000 layers) bottom flake and a thin (4-7 layers) top flake. Similar potential drops between the domains are observed independent of the thickness of the structures or the substrate: graphite ($SiO_2$) in A (C), respectively.

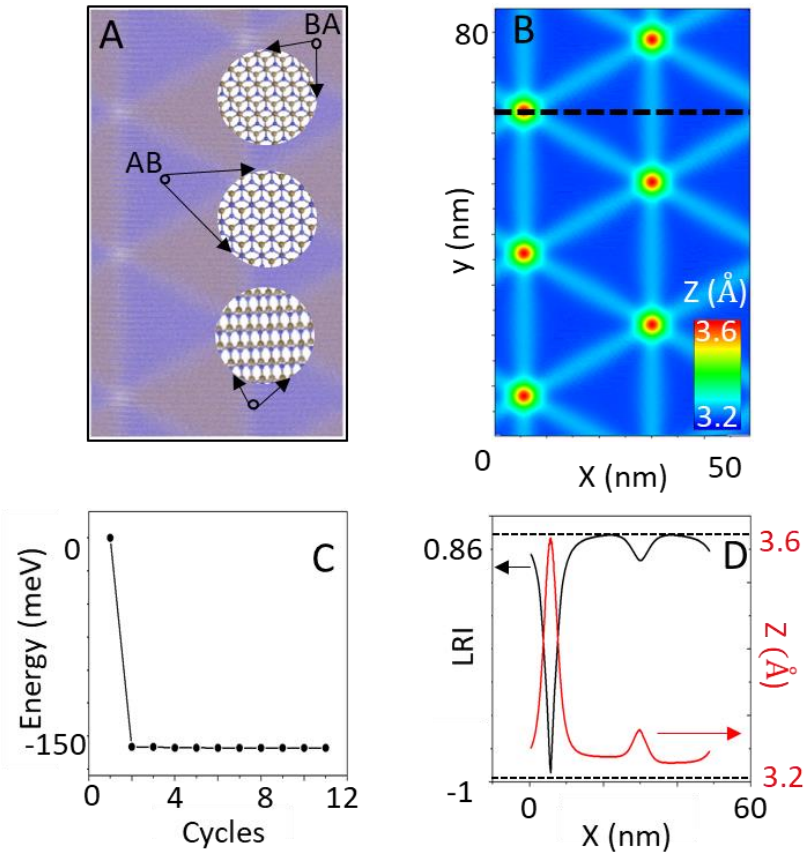


**Fig. S3**. **Geometric relaxation of the Moiré pattern**; (A) Atomic configuration of a relaxed periodic twisted bilayer *h*-BN with a twisted angle of $\theta = 0.5°$. The size of the entire model system is 48.9 nm × 84.7 nm. B and N atoms are colored by ochre and blue, respectively. Distinctly colored AB and BA domains are obtained since atoms of the upper layer hide those of the bottom layer that reside exactly below them. (B) Interlayer distance map for the relaxed twisted bilayer. (C) The energy variation during the minimization cycles applied to the model system appearing in panel (A) plotted relative to the initial energy. The first ten points represent cycles with force tolerance set to $10^{-3}$eV/Å and the last point corresponds to the final minimization step with force tolerance of $10^{-4}$eV/Å. (D) Interlayer distance (red) and local registry index (black) calculated along the path marked by the black dashed line in panel B. The reference LRI values of the AA and AB/BA stacking modes are -1 and 0.86 (marked by the corresponding horizontal lines).

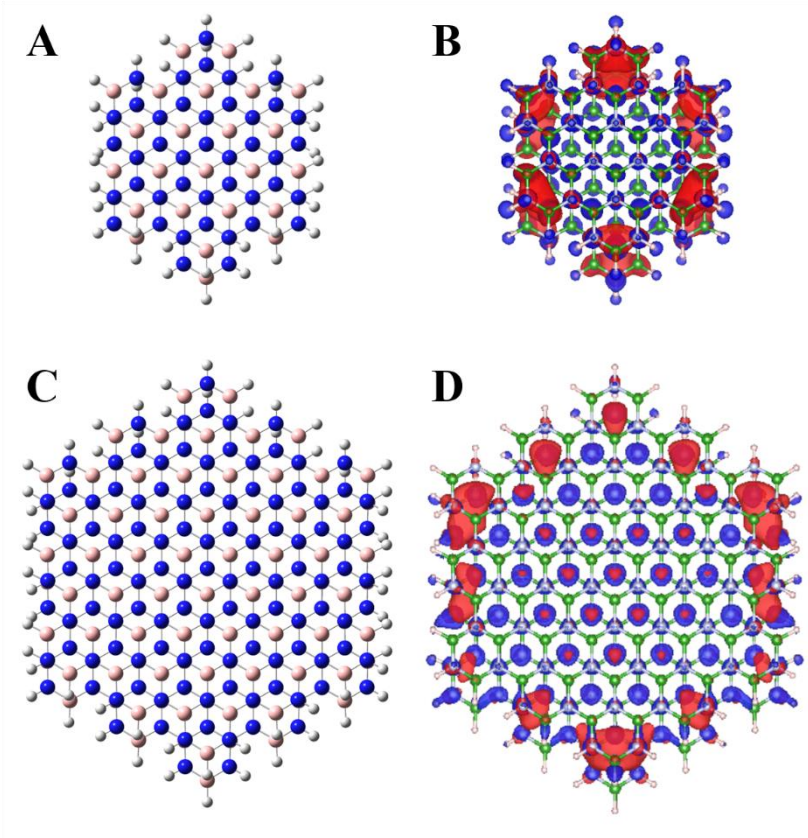


**Fig. S4. Charge distribution maps.** (A) Top view of the relaxed AB stacked hydrogen terminated finite bilayer *h*-BN flake of 1.1 $nm^2$ contact area. Pink, blue and white spheres represent boron, nitrogen, and hydrogen atoms, respectively. (B) The electron density difference (with respect to the isolated single-layered flakes) of the structure presented in (A) calculated at the B3LYP/Def2TZVP level of DFT theory. The blue and red color represent charge accumulation and depletion, respectively. The isosurface value is $2.3 \times 10^{-4}$ $e/Å^3$. (C) and (D) are same as (A) and (B) but for the 2.9 $nm^2$ contact area system, respectively.

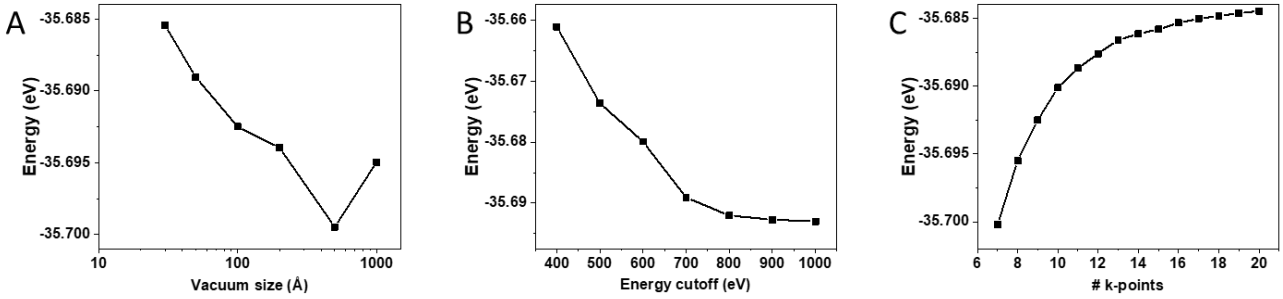


**Fig S5: Convergence tests**. Convergence tests of the total energy following geometry optimization as a function of (a) vacuum size; (b) energy cutoff; and (c) number of k-points.

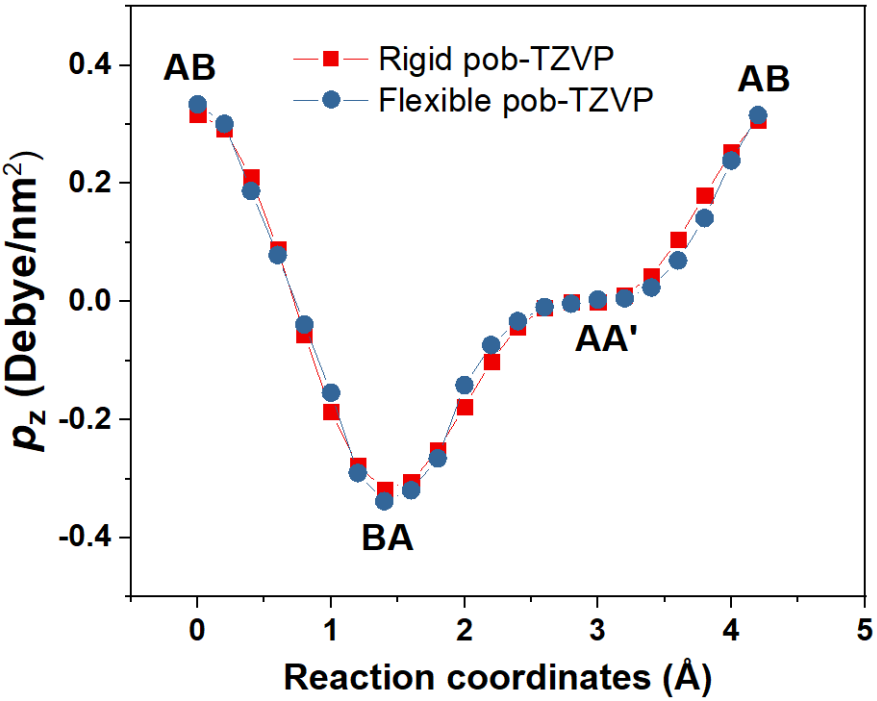


**Fig S6: Polarization as a function of lateral interlayer shift**. The out-of-plane polarization of bilayer *h*-BN as a function of interlayer displacement as calculated using the Gaussian package at the PBE/pob-TZVP level of theory for rigid and vertically flexible systems. The corresponding stacking modes are marked in the figure.

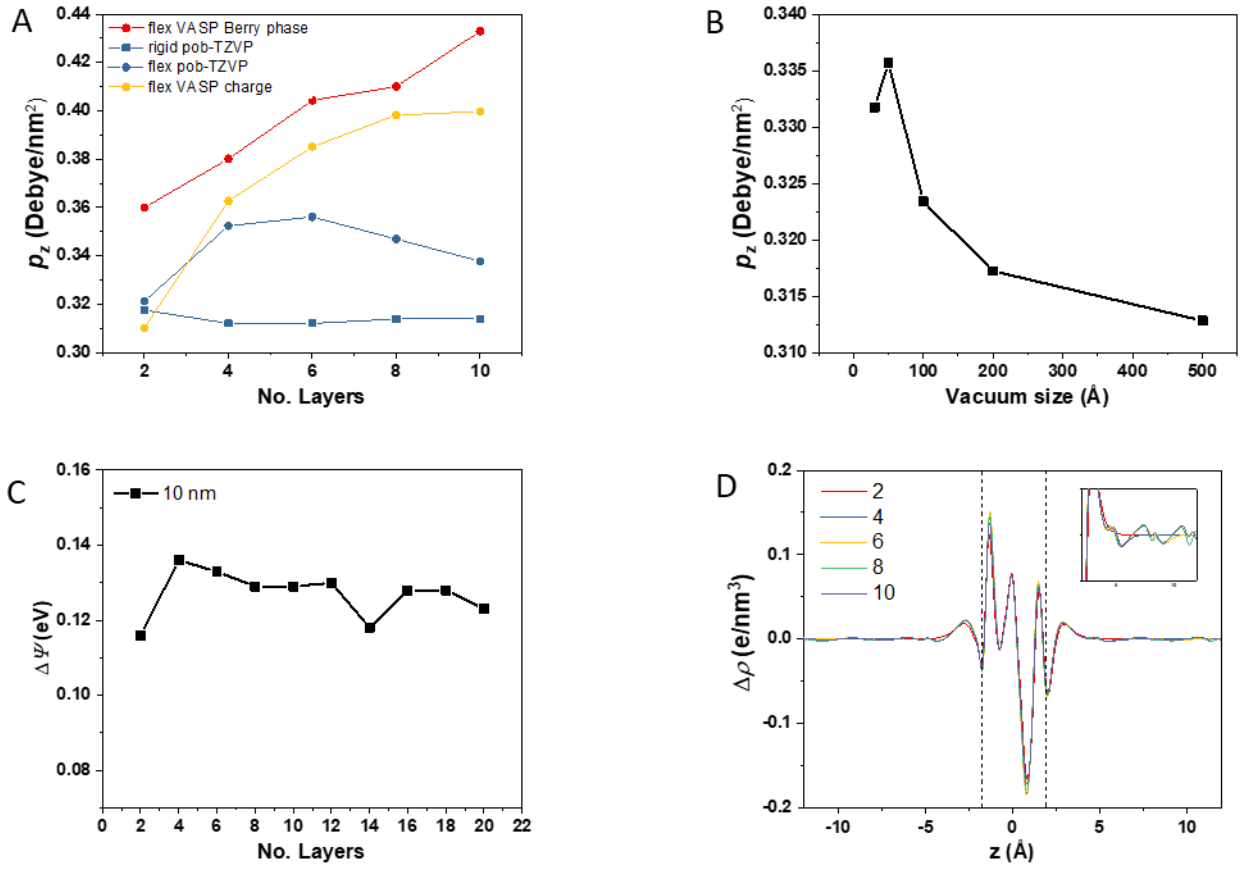


**Fig S7: Polarization dependence on the number layers** (a) The out-of-plane polarization as a function of the total number of layers calculated using three different methods (see section f.2.2): (i) the berry phase method in VASP with a 10 nm vacuum size (red); (ii) integration of charge density differences (yellow); and (iii) the Gaussian package at the PBE/pob-TZVP level of theory (blue). The multilayer system includes an AB stacked interface surrounded by two AA' stacked slabs (see text for full description). (b) The out-of-plane polarization as a function of vacuum size calculated by VASP for bilayer *h*-BN. (c) The electrostatic potential drop between the upper and lower surface as a function of number of layers. (d) The laterally summed charge density differences (with respect to the individual layers charge density) as a function of the vertical position (z) for several multilayer *h*-BN models ranging from the bilayer (red) to a 10-layer (gray) system. Zero vertical coordinate signifies the midpoint between the AB stacked central layers. The black dashed lines show the position of the AB stacked bilayer.

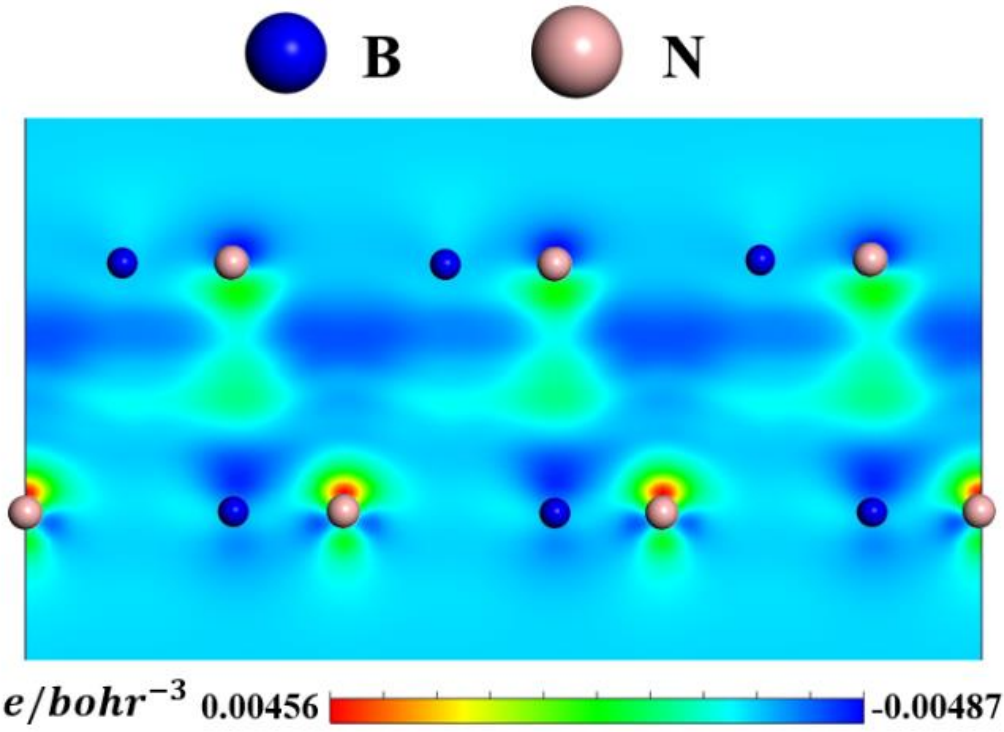


**Fig S8: Charge redistribution:** A two-dimensional cross section through the charge density differences (with respect to the individual layers) along the (110) crystallographic direction of the AB stacked bilayer *h*-BN calculated using VASP with the PBE density functional approximation.

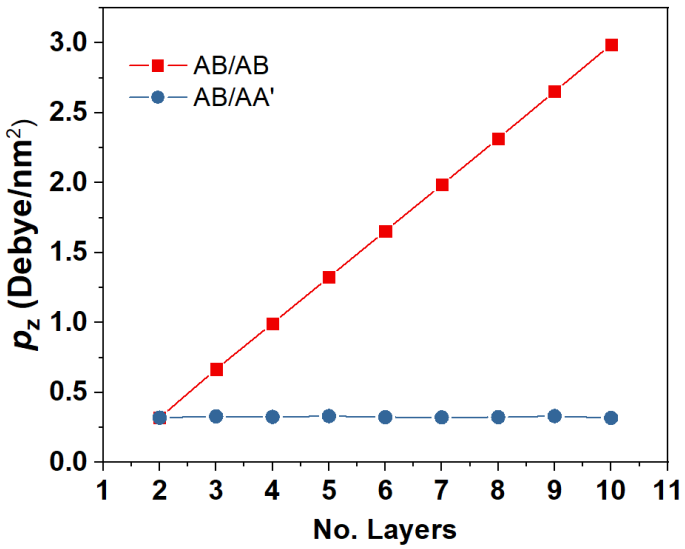


**Fig. S9. The out of plane polarization of an AB stacked multi-layer system.** The out-of-plane polarization as a function of number of layers for the fully AB stacked multilayer system (black squares) compared to the results presented in Fig. S7A above (red circles). The polarization was calculated using Gaussian.

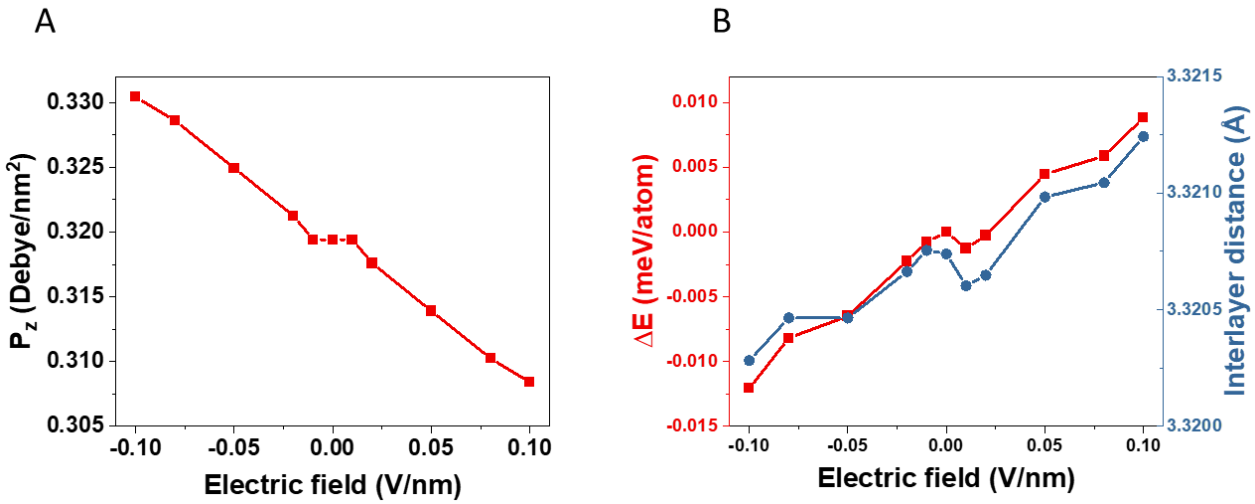


**Fig. S10. External electric field effects.** Field induced dipole moment (A, obtained using method (iii) of section f2.2), total energy, and interlayer distance (B) variation with an external electric field applied perpendicular to the interface of an AB stacked bilayer *h*-BN.

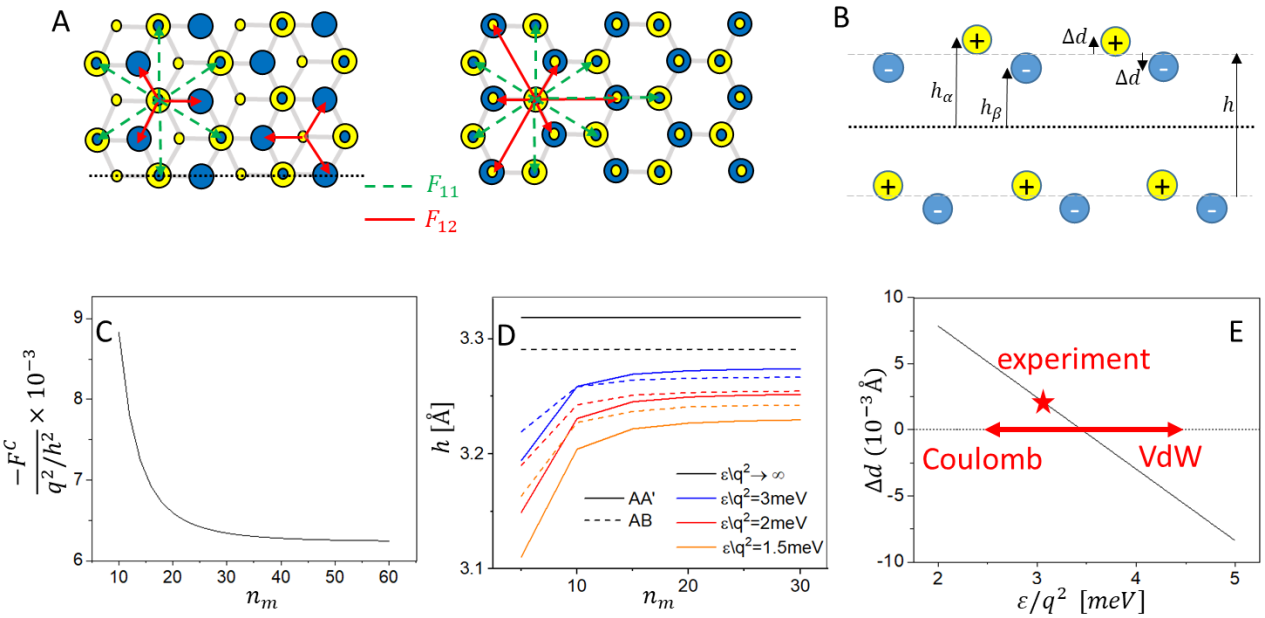


**Fig S11: Classical cohesion model.** (A) Top view of AB (left) and AA' (right) stacked bilayer *h*-BN. The top (bottom) layer atoms are marked by small (large) circles. Lattice sites that participate in the forces $F_{11\ (12)}$ in Eq. (S7, S8) are marked by dashed green (solid red) arrows, respectively. Similar to AA', the eclipsed atoms in AB experience both forces, however, the hollow atoms include only $F_{12}$ (twice). Also, note the zero Coulomb force in the latter case due to opposite charges of yellow/blue sites. (B) Cross-section of AB stacked bilayer *h*-BN along the dotted black line marked in (A). $\alpha(\beta)$ indicates hollow (eclipsed) sites, respectively. (C) Convergence of the total interlayer Coulomb force for $h = 3.3$ Å with the number of Bravais lattice vectors ($n_m$) in the summation in Eq. (S7, S8). (D) Inter-layer spacing ($h$) calculated for AA' (solid lines) and AB (dashed lines) stacked bilayer *h*-BN, for different fixed values of cohesion / Coulomb ratio $\varepsilon/q^2$. Black lines with $q = 0$ correspond to graphite and show smaller $h$ for AB than AA' stacking as expected, while orange lines with $\frac{\varepsilon}{q^2} = 1.5$meV show the opposite, as expected for *h*-BN. (E) Intra-layer displacement (marked in B) as a function of $\varepsilon/q^2$. The estimated value from the experiment is marked by a red star, suggesting $\varepsilon/q^2$~3 meV.

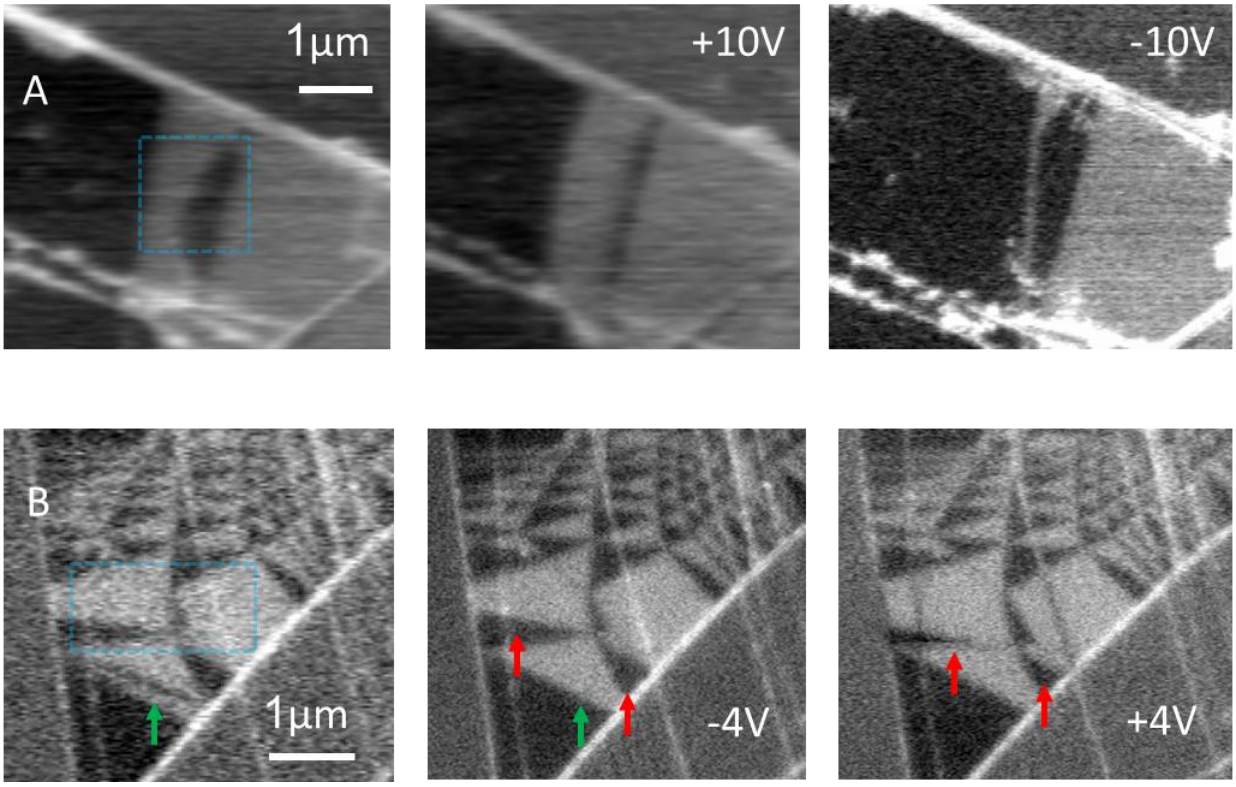


**Fig. S12. Additional examples of domain-wall sliding due to biased tip scans**. Consequent KPFM images from the left- to the right-hand side of the same flake location. (A) A biased tip (±10 V) was scanned above the region marked by a blue square. Positive tip bias resulted in domain-wall motion that increased the white domains area over the black domains and vice versa. The *h*-BN sandwich thickness is 14 nm above the graphite substrate. (B) A similar example with a tip biased ±4 V and *h*-BN thickness of 11 nm (see red arrows). Note the hybridization of domains at the green arrow position after the first scan. The expanding and narrowing of the domains does not depend on different scanning directions (up to down, left to right, and vice versa). The minimum flipping electric field measured is $\boldsymbol{0.3\ V/nm}$.

**References**


1. M. Lines, A. Glass, *Principles and applications of ferroelectrics and related materials* (2001; https://www.google.com/books?hl=en&lr=&id=p6ruJH8C84kC&oi=fnd&pg=PA1&dq=Principles+and+Applications+of+Ferroelectrics+and+Related+Materials+(Oxford+University.+Press,+1977)&ots=3F7179vH7T&sig=nefFtl1fv8lkap4UyS1S3QrVUro).
2. N. Setter, D. Damjanovic, L. Eng, G. Fox, S. Gevorgian, S. Hong, A. Kingon, H. Kohlstedt, N. Y. Park, G. B. Stephenson, I. Stolitchnov, A. K. Taganstev, D. V. Taylor, T. Yamada, S. Streiffer, Ferroelectric thin films: Review of materials, properties, and applications. *J. Appl. Phys.* **100** (2006), p. 051606.
3. J. F. Scott, [3D] nano-scale ferroelectric devices for memory applications. *Ferroelectrics*. **314**, 207–222 (2005).
4. J. F. Scott, Prospects for Ferroelectrics: 2012–2022. *ISRN Mater. Sci.* **2013**, 1–24 (2013).
5. M. Dawber, K. M. Rabe, J. F. Scott, Physics of thin-film ferroelectric oxides. *Rev. Mod. Phys.* **77**, 1083–1130 (2005).
6. J. Müller, P. Polakowski, S. Mueller, T. Mikolajick, Ferroelectric Hafnium Oxide Based Materials and Devices: Assessment of Current Status and Future Prospects. *ECS J. Solid State Sci. Technol.* **4**, N30–N35 (2015).
7. Y. Cao, A. Mishchenko, G. L. Yu, E. Khestanova, A. P. Rooney, E. Prestat, A. V. Kretinin, P. Blake, M. B. Shalom, C. Woods, J. Chapman, G. Balakrishnan, I. V. Grigorieva, K. S. Novoselov, B. A. Piot, M. Potemski, K. Watanabe, T. Taniguchi, S. J. Haigh, A. K. Geim, R. V. Gorbachev, Quality Heterostructures from Two-Dimensional Crystals Unstable in Air by Their Assembly in Inert Atmosphere (2015), doi:10.1021/ACS.NANOLETT.5B00648.
8. D. D. Fong, G. B. Stephenson, S. K. Streiffer, J. A. Eastman, O. Aucielo, P. H. Fuoss, C. Thompson, Ferroelectricity in ultrathin perovskite films. *Science (80-. ).* **304**, 1650–1653 (2004).
9. S. S. Cheema, D. Kwon, N. Shanker, R. dos Reis, S.-L. Hsu, J. Xiao, H. Zhang, R. Wagner, A. Datar, M. R. McCarter, C. R. Serrao, A. K. Yadav, G. Karbasian, C.-H. Hsu, A. J. Tan, L.-C. Wang, V. Thakare, X. Zhang, A. Mehta, E. Karapetrova, R. V Chopdekar, P. Shafer, E. Arenholz, C. Hu, R. Proksch, R. Ramesh, J. Ciston, S. Salahuddin, Enhanced ferroelectricity in ultrathin films grown directly on silicon. *Nature*. **580**, 478–482 (2020).
10. F. Liu, L. You, K. L. Seyler, X. Li, P. Yu, J. Lin, X. Wang, J. Zhou, H. Wang, H. He, S. T. Pantelides, W. Zhou, P. Sharma, X. Xu, P. M. Ajayan, J. Wang, Z. Liu, Room-temperature ferroelectricity in CuInP 2 S 6 ultrathin flakes. *Nat. Commun.* **7**, 1–6 (2016).
11. L. Li, M. Wu, Binary Compound Bilayer and Multilayer with Vertical Polarizations: Two-Dimensional Ferroelectrics, Multiferroics, and Nanogenerators. *ACS Nano*. **11**, 6382–6388 (2017).
12. G. Constantinescu, A. Kuc, T. Heine, Stacking in bulk and bilayer hexagonal boron nitride. *Phys. Rev. Lett.* **111** (2013), doi:10.1103/PhysRevLett.111.036104.
13. R. S. Pease, Crystal structure of boron nitride. *Nature*. **165**, 722–723 (1950).
14. S. Zhou, J. Han, S. Dai, J. Sun, D. J. Srolovitz, Van der Waals bilayer energetics: Generalized stacking-fault energy of graphene, boron nitride, and graphene/boron nitride bilayers. *Phys. Rev. B - Condens. Matter Mater. Phys.* **92**, 155438 (2015).
15. S. M. Gilbert, T. Pham, M. Dogan, S. Oh, B. Shevitski, G. Schumm, S. Liu, P. Ercius, S. Aloni, M. L. Cohen, A. Zettl, Alternative stacking sequences in hexagonal boron nitride. *2D Mater.* **6**, 021006 (2019).
16. J. H. Warner, M. H. Rümmeli, A. Bachmatiuk, B. Büchner, Atomic Resolution Imaging and Topography of Boron Nitride Sheets Produced by Chemical Exfoliation. *ACS Nano*. **4**, 1299–1304 (2010).
17. Materials, methods, and additional information are available as supplementary materials.
18. T. Maaravi, I. Leven, I. Azuri, L. Kronik, O. Hod, Interlayer Potential for Homogeneous Graphene and Hexagonal Boron Nitride Systems: Reparametrization for Many-Body Dispersion Effects. *J. Phys. Chem. C*. **121**, 22826–22835 (2017).
19. J. S. Alden, A. W. Tsen, P. Y. Huang, R. Hovden, L. Brown, J. Park, D. A. Muller, P. L. McEuen, Strain solitons and topological defects in bilayer graphene. *Proc. Natl. Acad. Sci. U. S. A.* **110**, 11256–11260 (2013).
20. M. R. Rosenberger, H. J. Chuang, M. Phillips, V. P. Oleshko, K. M. McCreary, S. V. Sivaram, C. S. Hellberg, B. T. Jonker, Twist Angle-Dependent Atomic Reconstruction and Moiré Patterns in Transition Metal Dichalcogenide Heterostructures. *ACS Nano*. **14**, 4550–4558 (2020).
21. A. Weston, Y. Zou, V. Enaldiev, A. Summerfield, N. Clark, V. Zólyomi, A. Graham, C. Yelgel, S. Magorrian, M. Zhou, J. Zultak, D. Hopkinson, A. Barinov, T. H. Bointon, A. Kretinin, N. R. Wilson, P. H. Beton, V. I. Fal'ko, S. J. Haigh, R. Gorbachev, Atomic reconstruction in twisted bilayers of transition metal dichalcogenides. *Nat. Nanotechnol.* **15**, 592–597 (2020).

22. H. Yoo, R. Engelke, S. Carr, S. Fang, K. Zhang, P. Cazeaux, S. H. Sung, R. Hovden, A. W. Tsen, T. Taniguchi, K. Watanabe, G.-C. Yi, M. Kim, M. Luskin, E. B. Tadmor, E. Kaxiras, P. Kim, Atomic and electronic reconstruction at the van der Waals interface in twisted bilayer graphene. *Nat. Mater.* |. **18**, 448–453 (2019).
23. T. A. Green, J. Weigle, Theorie du moire. *Helv. Phys. acta*. **21**, 217 (1948).
24. C. R. Woods, L. Britnell, A. Eckmann, R. S. Ma, J. C. Lu, H. M. Guo, X. Lin, G. L. Yu, Y. Cao, R. V. Gorbachev, A. V. Kretinin, J. Park, L. A. Ponomarenko, M. I. Katsnelson, Y. N. Gornostyrev, K. Watanabe, T. Taniguchi, C. Casiraghi, H.-J. Gao, A. K. Geim, K. S. Novoselov, Commensurate–incommensurate transition in graphene on hexagonal boron nitride. *Nat. Phys.* **10**, 451–456 (2014).
25. O. Hod, E. Meyer, Q. Zheng, M. Urbakh, Structural superlubricity and ultralow friction across the length scales. *Nature*. **563**, 485–492 (2018).
26. L. J. McGilly, A. Kerelsky, N. R. Finney, K. Shapovalov, E. M. Shih, A. Ghiotto, Y. Zeng, S. L. Moore, W. Wu, Y. Bai, K. Watanabe, T. Taniguchi, M. Stengel, L. Zhou, J. Hone, X. Zhu, D. N. Basov, C. Dean, C. E. Dreyer, A. N. Pasupathy, Visualization of moiré superlattices. *Nat. Nanotechnol.* **15**, 580–584 (2020).
27. P. Ares, T. Cea, M. Holwill, Y. B. Wang, R. Roldán, F. Guinea, D. V. Andreeva, L. Fumagalli, K. S. Novoselov, C. R. Woods, Piezoelectricity in Monolayer Hexagonal Boron Nitride. *Adv. Mater.* **32**, 1905504 (2020).
28. W. M. Lomer, K. W. Morton, The electrostatic energy of boron nitride [2]. *Proc. Phys. Soc. Sect. A.* **66**, 772–773 (1953).
29. Y.-N. Xu, W. Y. Ching, Calculation of ground-state and optical properties of boron nitrides in the hexagonal, cubic, and wurtzite structures. *Phys. Rev. B.* **44**, 7787–7798 (1991).
30. J.-C. Charlier, X. Gonze, J.-P. Michenaud, Graphite Interplanar Bonding: Electronic Delocalization and van der Waals Interaction. *Europhys. Lett.* **28**, 403–408 (1994).
31. N. Marom, J. Bernstein, J. Garel, A. Tkatchenko, E. Joselevich, L. Kronik, O. Hod, Stacking and registry effects in layered materials: The case of hexagonal boron nitride. *Phys. Rev. Lett.* **105** (2010), doi:10.1103/PhysRevLett.105.046801.
32. O. Hod, Graphite and hexagonal boron-nitride have the same interlayer distance. Why? *J. Chem. Theory Comput.* **8**, 1360–1369 (2012).
33. L. Jiang, S. Wang, Z. Shi, C. Jin, M. I. B. Utama, S. Zhao, Y. R. Shen, H. J. Gao, G. Zhang, F. Wang, Manipulation of domain-wall solitons in bi- and trilayer graphene. *Nat. Nanotechnol.* **13**, 204–208 (2018).
34. M. Yankowitz, J. I. J. Wang, A. G. Birdwell, Y. A. Chen, K. Watanabe, T. Taniguchi, P. Jacquod, P. San-Jose, P. Jarillo-Herrero, B. J. LeRoy, Electric field control of soliton motion and stacking in trilayer graphene. *Nat. Mater.* **13**, 786–789 (2014).
35. J. Sung, Y. Zhou, G. Scuri, V. Zólyomi, T. I. Andersen, H. Yoo, D. S. Wild, A. Y. Joe, R. J. Gelly, H. Heo, S. J. Magorrian, D. Bérubé, A. M. M. Valdivia, T. Taniguchi, K. Watanabe, M. D. Lukin, P. Kim, V. I. Fal'ko, H. Park, Broken mirror symmetry in excitonic response of reconstructed domains in twisted MoSe2/MoSe2 bilayers. *Nat. Nanotechnol.* **15**, 750–754 (2020).
36. T. I. Andersen, G. Scuri, A. Sushko, K. de Greve, J. Sung, Y. Zhou, D. S. Wild, R. J. Gelly, H. Heo, K. Watanabe, T. Taniguchi, P. Kim, H. Park, M. D. Lukin, Moiré excitons correlated with superlattice structure in twisted WSe2/WSe2 homobilayers. *arXiv* (2019) (available at http://arxiv.org/abs/1912.06955).
37. S. Artyukhin, K. T. Delaney, N. A. Spaldin, M. Mostovoy, Landau theory of topological defects in multiferroic hexagonal manganites. *Nat. Mater.* **13**, 42–49 (2014).
38. K. Yasuda, X. Wang, K. Watanabe, T. Taniguchi, P. Jarillo-Herrero, Stacking-engineered ferroelectricity in bilayer boron nitride. *arXiv* (2020) (available at http://arxiv.org/abs/2010.06600).
39. C. R. Woods, P. Ares, H. Nevison-Andrews, M. J. Holwill, R. Fabregas, F. Guinea, A. K. Geim, K. S. Novoselov, N. R. Walet, L. Fumagalli, Charge-polarized interfacial superlattices in marginally twisted hexagonal boron nitride. *Nat. Commun.* **12**, 1–7 (2021).
40. Z. Zheng, Q. Ma, Z. Bi, S. de la Barrera, M. H. Liu, N. Mao, Y. Zhang, N. Kiper, K. Watanabe, T. Taniguchi, J. Kong, W. A. Tisdale, R. Ashoori, N. Gedik, L. Fu, S. Y. Xu, P. Jarillo-Herrero, Unconventional ferroelectricity in moiré heterostructures. *Nature*. **588**, 71–76 (2020).
41. DOI for the SI.
42. C. R. Dean, A. F. Young, I. Meric, C. Lee, L. Wang, S. Sorgenfrei, K. Watanabe, T. Taniguchi, P. Kim, K. L. Shepard, J. Hone, Boron nitride substrates for high-quality graphene electronics. *Nat. Nanotechnol.* **5**, 722–726 (2010).
43. W. Melitz, J. Shen, A. C. Kummel, S. Lee, Kelvin probe force microscopy and its application. *Surf. Sci. Rep.* **66** (2011), pp. 1–27.
44. R. Borgani, D. Forchheimer, J. Bergqvist, P. A. Thorén, O. Inganäs, D. B. Haviland, Intermodulation

electrostatic force microscopy for imaging surface photo-voltage. *Appl. Phys. Lett.* **105** (2014), p. 143113.
45. J. Colchero, A. Gil, A. M. Baró, Resolution enhancement and improved data interpretation in electrostatic force microscopy. *Phys. Rev. B - Condens. Matter Mater. Phys.* **64**, 245403 (2001).
46. C. Sevik, A. Kinaci, J. B. Haskins, T. Çağın, Characterization of thermal transport in low-dimensional boron nitride nanostructures. *Phys. Rev. B*. **84**, 085409 (2011).
47. N. Marom, J. Bernstein, J. Garel, A. Tkatchenko, E. Joselevich, L. Kronik, O. Hod, Stacking and registry effects in layered materials: The case of hexagonal boron nitride. *Phys. Rev. Lett.* **105**, 046801 (2010).
48. I. Leven, R. Guerra, A. Vanossi, E. Tosatti, O. Hod, Multiwalled nanotube faceting unravelled. *Nat. Nanotechnol.* **11**, 1082–1086 (2016).
49. P. C. Hariharan, J. A. Pople, The influence of polarization functions on molecular orbital hydrogenation energies. *Theor. Chim. Acta*. **28**, 213–222 (1973).
50. M. J. Frisch, G. W. Trucks, H. B. Schlegel, G. E. Scuseria, M. A. Robb, J. R. Cheeseman, G. Scalmani, V. Barone, G. A. Petersson, H. Nakatsuji, X. Li, M. Caricato, A. Marenich, J. Bloino, B. G. Janesko, R. Gomperts, B. Mennucci, H. P. Hratchian, J. V. Ortiz, A. F. Izmaylov, J. L. Sonnenberg, D. Williams-Young, F. Ding, F. Lipparini, F. Egidi, J. Goings, B. Peng, A. Petrone, T. Henderson, D. Ranasinghe, V. G. Zakrzewski, J. Gao, N. Rega, G. Zheng, W. Liang, M. Hada, M. Ehara, K. Toyota, R. Fukuda, J. Hasegawa, M. Ishida, T. Nakajima, Y. Honda, O. Kitao, H. Nakai, T. Vreven, K. Throssell, J. A. Montgomery Jr., J. E. Peralta, F. Ogliaro, M. Bearpark, J. J. Heyd, E. Brothers, K. N. Kudin, V. N. Staroverov, T. Keith, R. Kobayashi, J. Normand, K. Raghavachari, A. Rendell, J. C. Burant, S. S. Iyengar, J. Tomasi, M. Cossi, J. M. Millam, M. Klene, C. Adamo, R. Cammi, J. W. Ochterski, R. L. Martin, K. Morokuma, O. Farkas, J. B. Foresman, D. J. Fox, Gaussian 09, Rev. D.01. *Gaussian Inc., Wallingford, CT* (2016).
51. S. Grimme, J. Antony, S. Ehrlich, H. Krieg, A consistent and accurate ab initio parametrization of density functional dispersion correction (DFT-D) for the 94 elements H-Pu. *J. Chem. Phys.* **132**, 154104 (2010).
52. F. Weigend, R. Ahlrichs, Balanced basis sets of split valence, triple zeta valence and quadruple zeta valence quality for H to Rn: Design and assessment of accuracy. *Phys. Chem. Chem. Phys.* **7**, 3297–3305 (2005).
53. G. Kresse, J. Furthmüller, Efficient iterative schemes for ab initio total-energy calculations using a plane-wave basis set. *Phys. Rev. B - Condens. Matter Mater. Phys.* **54**, 11169–11186 (1996).
54. J. P. Perdew, K. Burke, M. Ernzerhof, Generalized gradient approximation made simple. *Phys. Rev. Lett.* **77**, 3865–3868 (1996).
55. D. Joubert, From ultrasoft pseudopotentials to the projector augmented-wave method. *Phys. Rev. B - Condens. Matter Mater. Phys.* **59**, 1758–1775 (1999).
56. A. Ambrosetti, A. M. Reilly, R. A. Distasio, A. Tkatchenko, Long-range correlation energy calculated from coupled atomic response functions. *J. Chem. Phys.* **140**, 18A508 (2014).
57. P. Zhao, C. Xiao, W. Yao, Universal superlattice potential for 2D materials from twisted interface inside h-BN substrate. *arXiv* (2020) (available at http://arxiv.org/abs/2011.03933).
58. C. Kittel, Introduction to Solid State Physics, 8th edition. *Wiley Sons, New York, NY* (2004).
59. P. P. Gillis, Calculating the elastic constants of graphite. *Carbon N. Y.* **22**, 387–391 (1984).